ADVANCED MATERIALS
www.advmat.de

Magnetic Structure and Metamagnetic Transitions in the van der Waals Antiferromagnet $CrPS_4$

Yuxuan Peng, Shilei Ding, Man Cheng, Qifeng Hu, Jie Yang, Fanggui Wang, Mingzhu Xue, Zhou Liu, Zhongchong Lin, Maxim Avdeev, Yanglong Hou, Wenyun Yang, Yi Zheng,* and Jinbo Yang**

In 2D magnets, interlayer exchange coupling is generally weak due to the van der Waals layered structure but it still plays a vital role in stabilizing the long-range magnetic ordering and determining the magnetic properties. Using complementary neutron diffraction, magnetic, and torque measurements, the complete magnetic phase diagram of $CrPS_4$ crystals is determined. $CrPS_4$ shows an antiferromagnetic ground state (A-type) formed by out-of-plane ferromagnetic monolayers with interlayer antiferromagnetic coupling along the *c* axis below $T_N = 38$ K. Due to small magnetic anisotropy energy and weak interlayer coupling, the low-field metamagnetic transitions in $CrPS_4$, that is, a spin-flop transition at ≈0.7 T and a spin-flip transition from antiferromagnetic to ferromagnetic under a relatively low field of 8 T, can be realized for $H \| c$. Intriguingly, with an inherent in-plane lattice anisotropy, spin-flop-induced moment realignment in $CrPS_4$ for $H \| c$ is parallel to the quasi-1D chains of CrS_6 octahedra. The peculiar metamagnetic transitions and in-plane anisotropy make few-layer $CrPS_4$ flakes a fascinating platform for studying 2D magnetism and for exploring prototype device applications in spintronics and optoelectronics.

The emergence of van der Waals (vdW) magnets greatly enriched our understanding on intrinsic magnetism in the 2D limit, beyond the conventional Ising model and XY model pictures.[1–4] Different spin configurations in diverse materials enable the experimental realization of the well-established magnetism models. For example, Ising-type ferromagnetism (FM) is found in monolayer CrI_3,[1] while the XXZ-type antiferromagnetism (AFM) in bulk $NiPS_3$ is suppressed in monolayer $NiPS_3$,[5] both are consistent with the theoretical predictions.[6–8] Beyond these systems, 2D magnets with metamagnetic transitions, that is, a spin-flop or spin-flip transition from an AF state to a spin ferromagnetically polarized state,[9,10] are even more intriguing due to the potential of regulating and/or manipulating these transitions with extraordinary thickness-dependent phenomena. For instance, the spin-flop transition and realignment of magnetic moments from out-of-plane to in-plane AFM in $MnPS_3$[11] persist down to the monolayer regime. In few-layer antiferromagnet $CrCl_3$, spin-flop transitions show exotic even-odd layer dependence, in which an uncompensated layer in odd-layer samples leads to a finite spin-flop field.[12] These intriguing thickness-dependent metamagnetic phenomena evoke the pursuit of new types of vdW magnets, which will not only be helpful for the study of 2D magnetism but also enable the development of next-generation spintronic and optoelectronic devices.

$CrPS_4$ is a promising 2D antiferromagnetic semiconductor with bulk metamagnetic transition observed previously, which

Y. Peng, S. Ding, J. Yang, F. Wang, M. Xue, Z. Liu, Z. Lin, Prof. Y. Hou, Dr. W. Yang, Prof. J. Yang
State Key Laboratory for Artificial Microstructure & Mesoscopic Physics
School of Physics
Peking University
Beijing 100871, P. R. China
E-mail: yangwenyun@pku.edu.cn; jbyang@pku.edu.cn

M. Cheng, Q. Hu, Prof. Y. Zheng
Zhejiang Province Key Laboratory of Quantum Technology and Device
Department of Physics
Zhejiang University
Hangzhou 310027, P. R. China
E-mail: phyzhengyi@zju.edu.cn

The ORCID identification number(s) for the author(s) of this article can be found under https://doi.org/10.1002/adma.202001200.

DOI: 10.1002/adma.202001200

Prof. M. Avdeev
Australian Nuclear Science and Technology Organisation (ANSTO)
New Illawarra Road, Lucas Heights, Sydney, NSW 2234, Australia

Prof. Y. Hou, Prof. J. Yang
Beijing Key Laboratory for Magnetoelectric Materials and Devices
Beijing 100871, P. R. China

Prof. Y. Hou
Department of Materials Science and Engineering
College of Engineering
Peking University
Beijing 100871, P. R. China

Prof. J. Yang
Collaborative Innovation Center of Quantum Matter
Beijing 100871, P. R. China

was referred to as a magnetic switching effect.[13] Due to the weak interlayer vdW interactions along the *c* axis, $CrPS_4$ has already been exfoliated into monolayers.[14] Recent reports on 2D thin-film $CrPS_4$ flakes[14–18] are rather encouraging, with the discovery of unusual properties such as synaptic memory effects,[15] and Fano resonance below the Néel temperature due to the breaking of time-reversal symmetry.[18] However, to fully comprehend these interesting 2D magnetism-related phenomena, the debating magnetic structure of the bulk AFM in $CrPS_4$ crystals needs to be clarified first. Although $CrPS_4$ was first synthesized in 1977,[19] only a few studies have discussed the bulk magnetic structure. Pei et al. proposed a magnetic phase diagram of $CrPS_4$ with cubic-like nearest neighbor AFM alignments (G-type) as the ground state, which switches to a field-induced stripe-phased AFM (C-type) when field is along the *c* axis.[13] Two subsequent density functional theory (DFT) calculations suggested a zero field state of intralayer FM and interlayer AFM[20] (A-type AFM) and an antiferromagnetically coupled 1D FM chains phase in field,[21] respectively. These controversial results call for a study of intrinsic magnetic structure in bulk $CrPS_4$, which will greatly facilitate the understanding of layer-dependent magnetism in $CrPS_4$ thin flakes.

Here, we conducted complementary magnetic, torque, and neutron diffraction measurements to elucidate the metamagnetic transitions and the magnetic structure of high-quality $CrPS_4$ single crystals. By fitting of neutron diffraction results, an A-type AFM ground state is confirmed in bulk $CrPS_4$ below 38 K. When *H* is applied along the *c* axis ($H \| c$), a spin-flop transition is observed at around 0.7 T, corresponding to a canted interlayer AFM in the direction perpendicular to the *c* axis. The canted interlayer AFM phase eventually turns into out-of-plane ferromagnetic ordering, manifested by a spin-flip transition at about 8.5 T. In contrast, with in-plane applied magnetic field ($H \perp c$), there is no well-defined spin-flop transition, and the moment gradually rotates to the in-plane direction at nearly the same critical point of 8.5 T. These findings indicate a rather small interlayer antiferromagnetic exchange coupling, which may compete or correlate with the neutron-revealed in-plane magnetic anisotropy when dimensionality confinement comes into play. The existence of both spin-flop and canted AFM-to-FM/spin-flip transitions at relatively low fields makes $CrPS_4$ a unique platform for studying metamagnetic transitions in the 2D limit, which may lead to novel device applications using heterostructures, exchange bias, and electrostatic gating techniques.

Figure 1a exhibits the optical image of high-quality $CrPS_4$ single crystals, characterized by flat surfaces with metallic luster and in-plane crystal growth preference along the *b* axis. As shown in Figure 1b (visualized by VESTA[22]), the crystal structure of $CrPS_4$ has monoclinic symmetry with space group *C*2 (no. 5) and lattice constants of a = 10.85601(21) Å, b = 7.24732(14) Å, c = 6.13526(15) Å, β = 91.8840(11)° at room temperature. Since the majority of 2D magnets are monoclinic or rhombohedral,[23] it is worth noting that $CrPS_4$ could be regarded as an orthorhombic lattice considering the value of β is close to 90°. The sulfur atoms in $CrPS_4$ constitute the close-packed surface of individual monolayers with significant vdW gaps between them, allowing thin flakes or even monolayer to be readily obtained by micromechanical exfoliation.[14] Note that each monolayer of $CrPS_4$ can be viewed as quasi-1D chains of CrS_6 octahedra interconnected along the *a* axis, as schemed in Figure 1c.

As aforementioned, there is no direct experimental data for the magnetic structure of bulk $CrPS_4$. We have used neutron powder diffraction, one of the most straightforward techniques for determining materials' magnetic structure, to unravel the magnetic phase diagram of bulk $CrPS_4$. Typical neutron

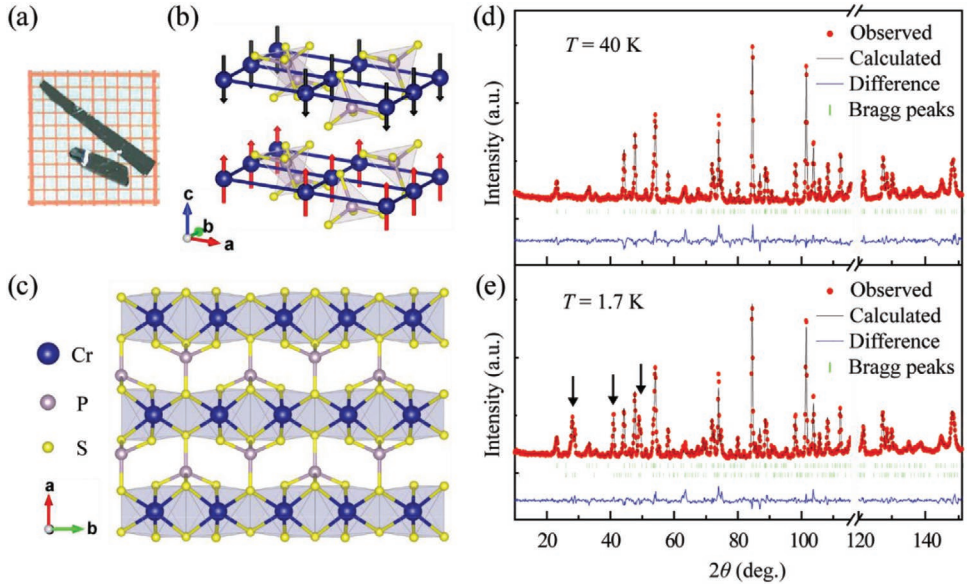

Figure 1. a) Optical image of $CrPS_4$ single crystals on a 1 mm grid paper. b) Crystal and magnetic structure of $CrPS_4$. The black and red arrows point to the direction of magnetic moments. c) The *a*-*b* plane of $CrPS_4$ monolayer. Chromium atoms form quasi-1D chains of CrS_6 octahedra along the *b* axis. d,e) Diffraction patterns of $CrPS_4$ powder sample at 40 and 1.7 K, respectively. The black arrows in (e) highlight the emergent magnetic diffraction peaks due to antiferromagnetic ordering. The green vertical marks from top to the bottom in (d) and (e) indicate the (*hkl*) positions of the nuclear and magnetic phases, respectively. Note that there is no structural phase transition in $CrPS_4$ down to 1.7 K.

diffraction patterns at 40 and 1.7 K, across the Néel temperature (T_N), are shown in Figure 1d,e, respectively. As indicated by the black arrows, three new reflections emerge in neutron diffraction at 1.7 K compared to that of 40 K (the subtraction of the two patterns is shown in Figure S1, Supporting Information), due to the ordering of magnetic moments below T_N. The neutron diffraction patterns are analyzed by the Rietveld technique using the FullProf computer code.[24,25] These magnetic reflections can be indexed with a propagation vector $\mathbf{k}$ = (0, 0, 0.5), which gives a doubled magnetic unit cell along c axis direction. Our refinement analyses support an A-type AFM order consisting of ferromagnetic monolayers coupled antiferromagnetically along the c axis, which is consistent with the previous theoretical calculation.[20] The determined magnetic structure is displayed in Figure 1b. The refined ordered moment is 2.864(28) μ_B, in which a dominant component of 2.844(28) μ_B is aligned to the c axis while a small portion of 0.477(94) μ_B is along the a axis. This means the moments are neither along c nor c^* (out-of-plane) axis. The existence of titled magnetic moments with respect to the crystal axes may indicate the presence of competing anisotropies.[26] Due to the small titled angle from the c axis, the moments are considered to be along the c axis for convenience.

Figure 2a shows the zero-field-cooled (ZFC) magnetization characteristics of $CrPS_4$ single crystal for H = 1 kOe parallel and perpendicular to the c axis, respectively. The Néel temperature T_N, manifested as a kink in the ZFC curve, is observed at around 38 K, which is slightly higher than the reported 36 K in the earlier studies[13,27] but consistent with 37.9 K in recent studies.[14,28] The smaller magnetization (M) for $H\|c$ below the T_N is due to a bulk easy axis along the c direction. By fitting the high-temperature data (above 100 K) for $H\|c$ to the Curie–Weiss's law, we obtain the Weiss temperature T_θ = 41.6 K. The resulting positive T_θ indicates predominantly ferromagnetic coupling between moments, which is consistent with the A-type AFM model, in which neighboring Cr moments form ferromagnetic interaction in the a–b plane before the bulk AFM transition. Figure 2b–d shows the field-dependent magnetization curves at different temperatures for $H\|c$ and $H\perp c$, respectively. Distinctively, the M-curve for $H\|c$ at 2 K shows a typical AFM feature with infinitesimal magnetic susceptibility in low field. However, by increasing H to around 0.7 T, the magnetization shows a sharp and nonlinear increase, indicating a field-induced spin-flop phase transition. Following the phase transition, the magnetization linearly grows as a function of H and eventually becomes saturated above 8 T. Such M–H behavior is typical for the rotation of canted spin momentums in external field, and the saturation moment is equivalent to ≈2.61μ_B per Cr, consistent with the neutron diffraction result above. The smaller value obtained from the magnetic measurements is likely due to the residual canting even when the magnetization shows saturation behavior at the highest field of 9 T. For $H\perp c$, no low-field metamagnetic transition is observed, although the linear

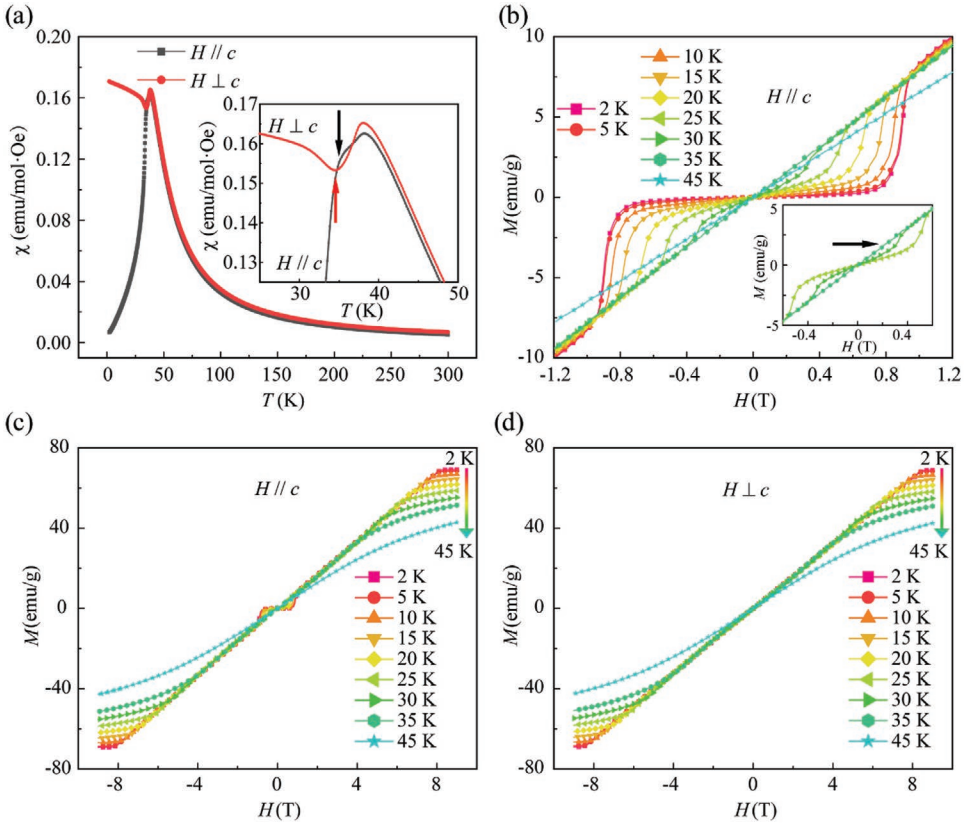

Figure 2. a) Zero-field-cooled magnetic susceptibilities of $CrPS_4$ single crystal with 1 kOe field applied in parallel and perpendicular to the crystallographic c axis. Inset shows the zoom-in image of observed anomalies around 35 K. b,c) Field-dependent magnetization at different temperatures with field parallel to the c axis. The inset of (b) shows the zoom-in image of the absent spin-flop transition at 35 K indicated by the black arrow. d) Field-dependent magnetization at different temperatures with field perpendicular to the c axis.

M growth and the high-field saturation behavior are retained. The situation is rather different for $H\|c$, in which canted AFM is formed by a reconstruction of spin moment alignment from out-of-plane (bulk easy axis) to in-plane geometries since the anisotropy energy is relatively small.[29]

Noticeably, as temperature increases, the spin-flop field (H_{SF}) for $H\|c$ dwindles and vanishes at 35 K (Figure 2b), which is related to the temperature scaling of anisotropy energy (K_μ) by $H_{SF} \propto \sqrt{K_\mu}$.[30–32] It is also noteworthy that there is an abnormal minimum around 35 K in the M (T) curve for $H\perp c$ (inset of Figure 2a), where spin-flop transition already disappears. To get insights into this anomaly, we have measured M (T) curves under different in-plane fields, which show that the dip point moves to lower temperatures as in-plane field increases and becomes completely suppressed at 5 T (Figure S2, Supporting Information). Based on these observations, it is likely that this abnormal M (T) behavior for $H\perp c$ is induced by in-plane short-range ferromagnetic correlations, competing with out-of-plane AFM ordering. Similar phenomena have been observed in $CrCl_3$, although short-range ferromagnetic correlations form well before long-range antiferromagnetic order developing.[33,34]

The magnetic properties of $CrPS_4$ were further investigated by metal-cantilever based torque magnetometer, which directly probes the anisotropy of magnetic susceptibility in crystalline materials.[32,35] In general, the magnetic torque $\vec{\tau}$ can be expressed as $\vec{\tau} = \mu_0 (\vec{M} \times \vec{H})$. In the case of an antiferromagnet with uniaxial anisotropy, the magnetic torque is derived from the magnetic anisotropy of the ordered magnetic moments.[30] The free energy F of the system can be formulated by[30–32,35,36]

$$F = -\frac{1}{2}\left[\chi_\perp \sin^2(\phi) + \chi_\| \cos^2(\phi)\right]\mu_0 H^2 + K_\mu \sin^2(\phi - \theta) \quad (1)$$

where $\chi_\perp$ and $\chi_\|$ are the susceptibilities in perpendicular and parallel to the easy axis, respectively, θ is the angle between H and the easy axis, φ is the angle between H and the spin axis. By definition, the torque force can be calculated by

$$\tau = -\frac{\partial F}{\partial \theta} = \frac{1}{2}(\chi_\perp - \chi_\|)\mu_0 H^2 \frac{\sin(2\theta)}{\sqrt{\lambda^2 - 2\lambda\cos(2\theta) + 1}} \quad (2)$$

Here, λ is defined by $\lambda = \left(\frac{H}{H_{SF}}\right)^2$ in which the spin-flop field H_{SF} is

$$H_{SF} = \sqrt{\frac{2K_\mu}{\mu_0(\chi_\perp - \chi_\|)}} \quad (3)$$

Figure 3a compares the magnetic torque of $\theta = 10°$ and 80° at 2 K (the torque measurement configuration is sketched in the inset). When the applied field is nearly parallel to the c axis ($\theta = 10°$), the magnetic torque is positive at low fields,

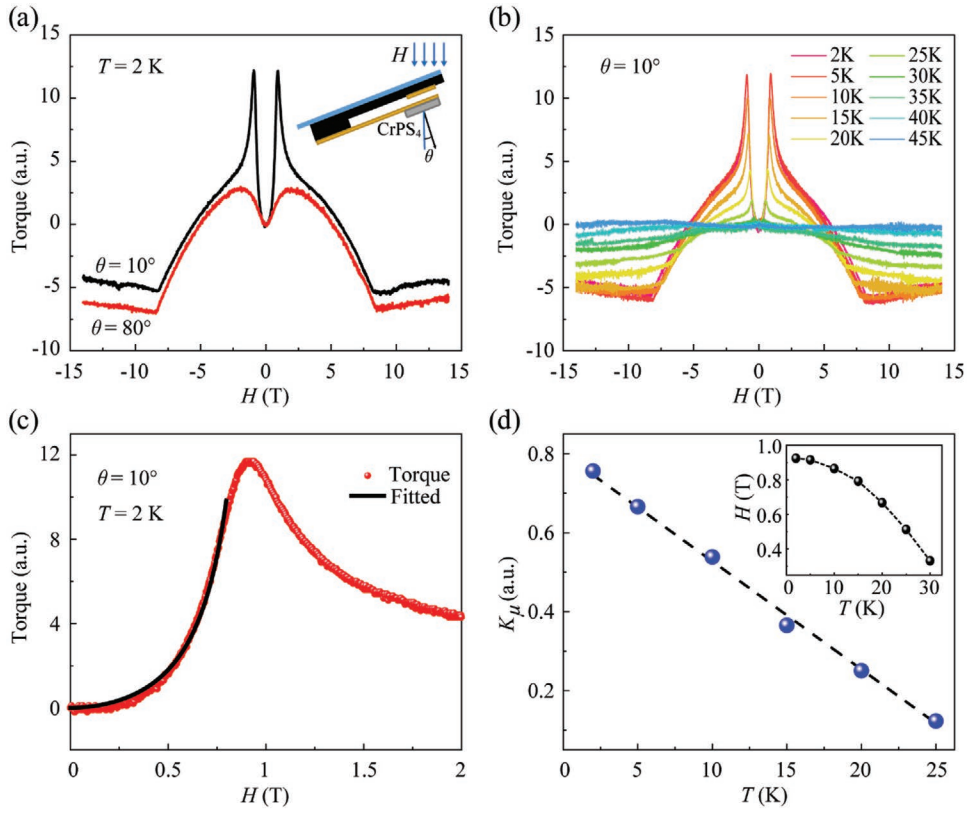

Figure 3. a) Magnetic torque of $\theta = 10°$ and 80° at 2 K. The schematic diagram of the measurement is shown in the inset. b) Magnetic torque of $\theta = 10°$ at different temperatures. The sharp torque peaks correspond to spin-flop transitions, allowing $H_{SF}(T)$ to be determined precisely. c) Low-field torque of $\theta = 10°$ at 2 K and the fitting result by using Equation (2). d) The fitted anisotropy energy K_μ of $\theta = 10°$ using data in (b). The dashed line is the linear fitting of the anisotropy energy. Inset: the spin-flop fields at different temperature extracted from (b).

suggesting $\chi_\perp > \chi_\parallel$ and an easy magnetization axis along the *c* axis. Above $H_{SF} = 0.91$ T, there is a steep drop in the torque signals, as a result of a spin-flop transition when the out-of-plane interlayer AFM ground state becomes canted in perpendicular to the *c* axis. The transition causes pronounced field-dependent changes in $\chi_\parallel$ with respect to $\chi_\perp$, and the toque force turns negative when $\chi_\parallel$ exceeds $\chi_\perp$ at around 5 T. In the following regime, the tilted spins gradually rotate to the *c* direction as driven by the external field, and the magnetization reaches a saturation point at 8.16 T, manifested as a distinctive kink when the slope of the torque signals get a positive sign again. In contrast, when *H* is nearly in plane ($\theta = 80°$), there is no well-defined AFM-to-spin flop transition since the in-plane component of *H* (H_{ab}) is dominating over the out-of-plane one (H_c). As the field increases, the instantly canted spins gradually rotate to the field direction and saturate at 8.46 T. These results are in excellent agreement with the *M*–*H* results.

Figure 3b shows the *T*-dependent magnetic torque at $\theta = 10°$. The ultra-sensitivity of torque force to the anisotropic changes in magnetic susceptibility makes the dwindling of spin flops conspicuous in $\tau(H)$ curves, which also shows remarkable consistency with the magnetic measurements on the spin-flop quenching point of 35 K. By fitting the low-field quadratic part of $\tau(H)$ to Equation (2), we are able to extract *T*-dependent K_μ, as exemplified by the fitting result of 2 K shown in Figure 3c. As summarized in Figure 3d, the anisotropy energy K_μ decreases monotonically with increasing temperature (black dashed line), which is in agreement with the evolution of the spin-flop field H_{SF}(T) shown in the inset.

In order to get insights into the metamagnetic transitions, we conducted field-dependent neutron powder diffraction to clarify the evolution of magnetic structures in field (see Experimental Section for details). Uniquely, neutron experiments allow us to clearly differentiate nuclear diffraction peaks, which barely change in external field, from field-dependent magnetic diffraction peaks. As shown in **Figure 4**a, by plotting the 2D intensity map of neutron diffraction patterns as a function of both diffraction angle (2θ) and field (H), it is straightforward to see the correlation between the evolution of metamagnetic states and magnetic diffraction peaks. Together with zoom-in spectra shown Figure 4b, it is clear that all diffraction peaks at 0.6 T are nearly the same as 0 T, since there is no metamagnetic transition until 0.7 T. At 1.2 T, the magnetic diffraction peaks change pronouncedly, while the nuclear diffraction peaks (for example $(220)_N$) are almost unchanged. At 9.0 T, the original magnetic diffraction peaks disappear, and a series of new peaks emerge, due to the formation of a saturated FM structure. For magnetic scattering peaks, the spin-flop transition at 0.7 T activates a strong selection rule for the peak intensity: the peaks indexed by (*hkl*) are suppressed only when $k \neq 0$, while they are slightly enhanced for $k = 0$ in comparison with the case of 0.6 T. The result strongly suggests that the *c* axis aligned magnetic moments in the ground state have rotated to the *b* axis at 1.2 T. Therefore, as illustrated in Figure 4e, the essence of the low-field metamagnetic transition for $H \| c$ can be concluded that magnetic moments in the ground state switch to the *b* axis, which corresponds to the direction of the quasi-1D chains of CrS_6 octahedra in the vdW plane. Such field-induced behavior is typical for a spin-flop transition, during which the ground-state magnetic moments will turn to the direction perpendicular to the magnetic field applied along the easy axis.

As the samples used in the neutron diffraction are powders, the orientations of micro-flakes in the sample are random. Hence, significant portions of micro-flakes do not undergo the field-induced phase transition when the effective magnetic field component along the *c* axis of individual flakes is lower than the spin-flop field of 0.7 T. Therefore, we have used two magnetic structure models to refine the neutron diffraction pattern at 1.2 T. One is the ground-state magnetic structure with moments along the *c* axis (without spin-flop transition), the other is the magnetic structure with moments distributed along the *b* axis (after spin-flop transition). The canted moments along the magnetic field direction is neglected since the net magnetization observed in *M*–*H* curves is small. As shown in Figure 4c, the calculated pattern is in excellent agreement with the experimental spectrum. This verifies the validity of our analysis, confirming that the spin-flop transition in $CrPS_4$ for $H \| c$ is realized by moments rearrangement from antiferromagnetically aligned along the *c* axis to antiferromagnetically canted along the *b* axis.

We have also refined the neutron diffraction data at 9 T to understand the high-field magnetic structure. As shown in Figure 4d, the high-field magnetic reflections are indexed with a propagation vector $\mathbf{k} = (0, 0, 0)$, which strongly supports that the magnetic structure at 9 T is a FM-like ordered structure. Using the ferromagnetic structure model, the refined magnetic moment components of Cr atoms along three different crystallographic axes are $m_a = 1.17(13)\ \mu_B$, $m_b = 0.95(19)\ \mu_B$, and $m_c = 2.38(7)\ \mu_B$, respectively. Note that the microflakes in the sample are arranged randomly, so the direction of polarized magnetic moments with respect to crystallographic axes in each microflakes should be different under the external magnetic field. Therefore, the neutron refinement results can only be considered as statistical averages. The results indicate that at 9 T the magnetic structure of $CrPS_4$ is a FM-like ordered structure with all the moments polarized along the external magnetic field, manifested as the saturation behavior observed in the magnetic and torque measurements of $CrPS_4$ single crystals at high magnetic fields. Our DFT calculations reveal that the cohesive energy difference between the AFM ground state and the FM ordering is only 4.5 meV, which accounts for the small spin-flip field (Table S1, Supporting Information). The schematic evolution of the magnetic structure with increasing magnetic field applied along the *c* axis is summarized in Figure 4e.

Based on these complementary magnetic measurements, we can now establish the complete magnetic phase diagram of bulk $CrPS_4$ for $H \| c$. As shown in **Figure 5**, four regions are delineated: 1) the paramagnetic phase above T_N; 2) the A-type antiferromagnetic ground state in low fields below T_N; 3) the canted antiferromagnetic (CAFM) phase in which magnetic moments are aligned antiferromagnetically along the *b* axis with small net moments along the field; and 4) the ferromagnetic-like phase at fields high enough to overcome the antiferromagnetic exchange coupling. As shown in the torque measurements, magnetic anisotropy energy decreases with increasing temperature. Since the spin-flop transition field is given by $H_{SF} \propto \sqrt{K_\mu}$, the critical field between A-AFM and CAFM decreases as temperature increases and eventually

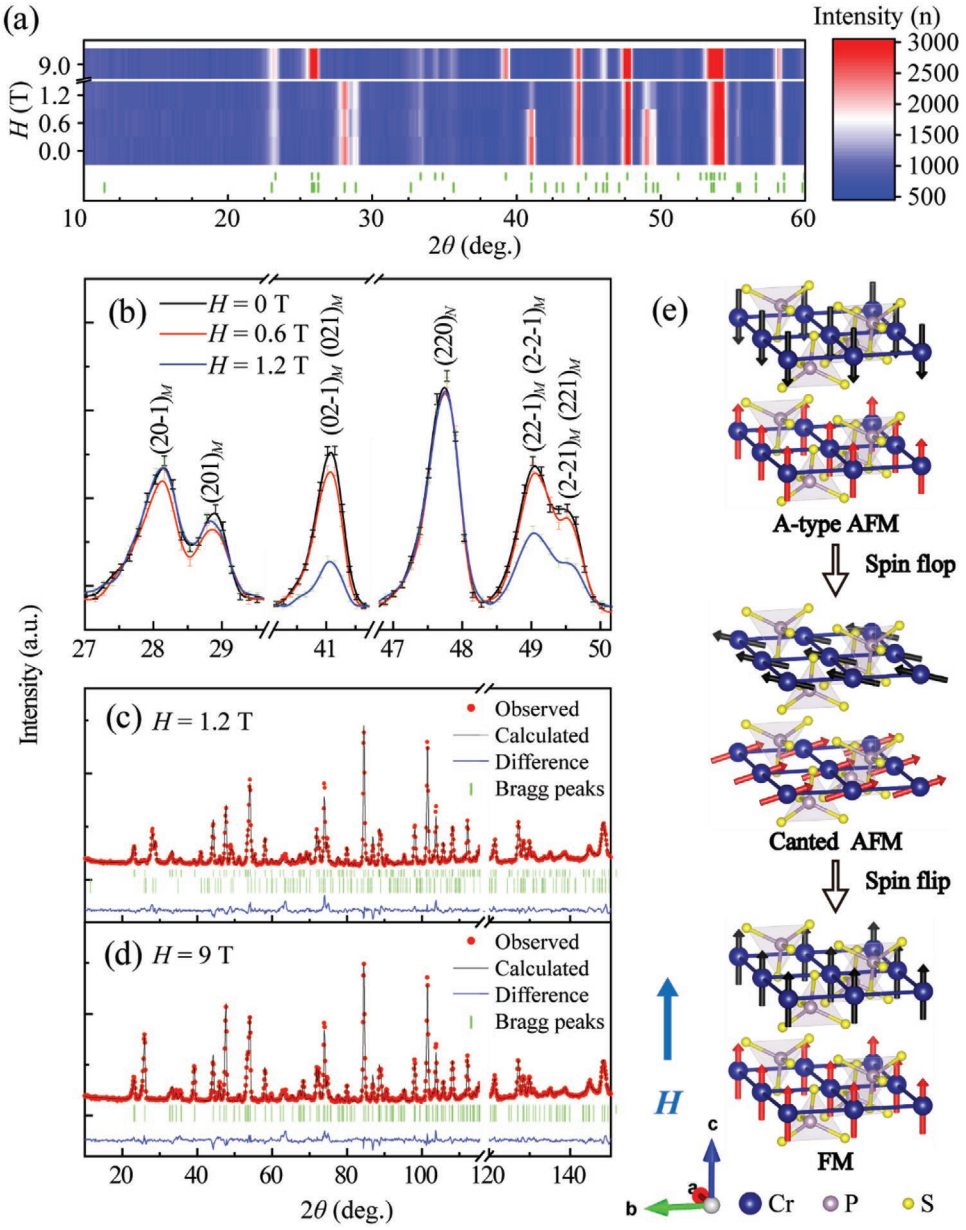

Figure 4. a–d) Neutron diffraction patterns at 1.7 K with different magnetic fields. e) The evolution of magnetic structure with increasing applied magnetic field along the *c* axis. The green vertical marks from the top to the bottom in (a), (c), and (d) indicate the (*hkl*) positions of the nuclear and magnetic phases, respectively.

vanishes at ≈35 K. As the applied magnetic fields suppress the antiferromagnetic correlations,[9] the critical temperature from the CAFM phase to the ferromagnetic-like phase also decreases with increasing fields.[34] The boundary between the FM and PM phases is defined by the Néel temperature T_N = 38 K, where spin-flip transition disappears as shown in Figure 2c.

In summary, we have presented a comprehensive investigation on the magnetic structures and metamagnetic transitions of vdW $CrPS_4$ crystals. Using complementary neutron diffraction, DC magnetization and cantilever-based torque measurements, we prove an A-type AFM ground state with intralayer ferromagnetic ordering and interlayer antiferromagnetic coupling for $CrPS_4$ crystals below T_N = 38 K. For $H \| c$, a spin-flop transition occurs when the out-of-plane aligned moments suddenly switch to a CAFM geometry along the *b* axis at around 0.7 T. After the spin-flop transition, the moments then gradually rotate and eventually flip to the field direction at around 8 T. Compared with other known A-type vdW antiferromagnets, $CrPS_4$ crystals are distinctive by the relatively small spin-flop field and the low CAFM-FM threshold, both are rooted in the weak interlayer coupling between neighboring monolayers and low magnetic anisotropy energy. By reducing the dimensionality, these metamagnetic transitions may interplay dynamically with the inherent in-plane lattice anisotropy, providing unprecedented opportunities for the study of exotic field-induced metamagnetic transitions in the 2D limit and for developing

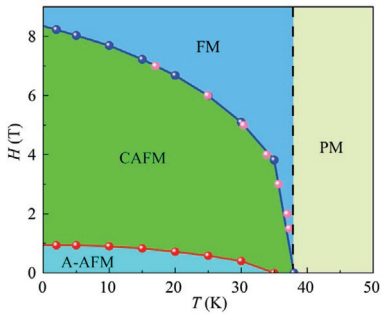

Figure 5. Magnetic phase diagram of $CrPS_4$ with applied field along the *c* axis. The red and blue balls are extracted from the *M*(*H*) curves shown in Figure 2. Pink balls are extracted from the *M*(*T*) curves. The black dashed line is for a potential boundary between the FM and PM phases at $T_N = 38$ K.

conceptual device applications in spintronics and optoelectronics. Indeed, layer-dependent study of 2D magnetic crystals, such as CrI_3,[1,37,38] $CrCl_3$,[12,39] and $MnBiTe_3$,[40–42] has not only enriched our fundamental understanding on 2D magnetism, but also revealed many exciting low-dimensional physical phenomena like the even-odd effect in spin-flop transitions.

Experimental Section

Sample Preparation and Characterization: The $CrPS_4$ single crystals were grown using chemical vapor transport (CVT) method. Chromium powders, red phosphorus, and sulfur powders from Alfa Aesar (99.99%) were weighed and mixed in stoichiometric ratio 1:1:4 with additional iodine as transport agents. These starting materials were sealed in a quartz tube before loading into a two-zone furnace. During the growth, the source end was kept at 953 K, and the sink was kept at 873 K for 8 days. After CVT growth, $CrPS_4$ single crystals were obtained on the sink side of the quartz tube. The structure of $CrPS_4$ single crystals was investigated by an X'Pert Pro MPD diffractometer with Cu Kα radiation (λ = 1.5418 Å). The DC magnetization measurements were performed using a vibrating sample magnetometer (VSM) module in a Quantum Design Physical Properties Measurement System (PPMS-9T).

Magnetic Torque Measurements: Torque magnetometry measurements were carried out in a capacitor geometry, formed by a bottom gold (Au) sheet and a top Au cantilever for mounting single-crystal samples with predetermined crystalline axes on the free end. The field-dependent torque force induces a deflection of the cantilever and a minute change in the capacitance signals, which are precisely detected by an atto-farad (aF) capacitance bridge.

Neutron Diffraction Measurements: The neutron diffraction data were collected using the ECHIDNA high-resolution powder diffractometer at the Australian Nuclear Science and Technology Organisation (ANSTO) with an incident neutron wavelength of 2.4395(2) Å. Temperature-and-field-dependent diffraction patterns were obtained from 1.7 to 300 K with a maximum magnetic field of 9 T. In order to reduce the influence of preferred orientation on the neutron diffraction measurement, we first crushed and milled the single crystals into powders (microflakes) to obtain reflections from different crystal planes, and then compressed the powdery microflakes into a cylinder so that the microflakes in the samples did not rotate when a strong magnetic field was applied. The preferred orientation function, Modified March's function (FullProf code Nor = 1)[24,25] is used to account for the prefer orientation effect. The neutron powder diffractometer used has the Debye–Scherrer geometry and the obtained preferred orientation parameter G1 is 1.7697, consistent with the layered nature of the sample.

Theoretical Calculations: DFT calculations were carried out in the Vienna Ab initio Simulation Package (VASP).[43] The generalized gradient approximation by Perdew, Burke, and Ernzerhof was used to get exchange and correlation interaction.[44,45] All calculations are based on a supercell of 1 × 1 × 2. The vdW-D2 approach is used to incorporate vdW interaction. The energy cutoff for the plane wave expansion was set to 500 eV. The Monkhorst–Pack *k*-point mesh was sampled with a separation of 0.01 $Å^{-1}$ in the Brillouin zone. The ionic relaxation stops when the energy difference and the residual force on each atom are less than 1×10^{-6} eV and 0.001 eV $Å^{-1}$, respectively. The spin-orbit coupling effect is included.

Supporting Information

Supporting Information is available from the Wiley Online Library or from the author.

Acknowledgements

Y.P., S.D., and M.C. contributed equally to this work. This work was supported by the National Key R&D Program of China (grant nos. 2017YFA0206303 and 2016YFA0300204) and the National Natural Science Foundation of China (grant nos. 11975035, 51731001, and 11574264).

Conflict of Interest

The authors declare no conflict of interest.

Keywords

2D antiferromagnets, magnetic insulators, magnetic structures, metamagnetic transitions, spintronics

Received: February 20, 2020
Revised: April 19, 2020
Published online:

[1] B. Huang, G. Clark, E. Navarro-Moratalla, D. R. Klein, R. Cheng, K. L. Seyler, D. Zhong, E. Schmidgall, M. A. McGuire, D. H. Cobden, W. Yao, D. Xiao, P. Jarillo-Herrero, X. Xu, *Nature* **2017**, *546*, 270.
[2] C. Gong, L. Li, Z. Li, H. Ji, A. Stern, Y. Xia, T. Cao, W. Bao, C. Wang, Y. Wang, Z. Q. Qiu, R. J. Cava, S. G. Louie, J. Xia, X. Zhang, *Nature* **2017**, *546*, 265.
[3] Z. Fei, B. Huang, P. Malinowski, W. Wang, T. Song, J. Sanchez, W. Yao, D. Xiao, X. Zhu, A. F. May, W. Wu, D. H. Cobden, J. H. Chu, X. Xu, *Nat. Mater.* **2018**, *17*, 778.
[4] Y. Deng, Y. Yu, Y. Song, J. Zhang, N. Z. Wang, Z. Sun, Y. Yi, Y. Z. Wu, S. Wu, J. Zhu, J. Wang, X. H. Chen, Y. Zhang, *Nature* **2018**, *563*, 94.
[5] K. Kim, S. Y. Lim, J. U. Lee, S. Lee, T. Y. Kim, K. Park, G. S. Jeon, C. H. Park, J. G. Park, H. Cheong, *Nat. Commun.* **2019**, *10*, 345.
[6] L. Onsager, *Phys. Rev.* **1944**, *65*, 117.
[7] J. M. Kosterlitz, D. J. Thouless, *J. Phys. C: Solid State Phys.* **1973**, *6*, 1181.
[8] V. Berezinskii, *Sov. Phys. - JETP* **1971**, *32*, 493.
[9] J. L. Luo, N. L. Wang, G. T. Liu, D. Wu, X. N. Jing, F. Hu, T. Xiang, *Phys. Rev. Lett.* **2004**, *93*, 187203.
[10] R. S. Perry, L. M. Galvin, S. A. Grigera, L. Capogna, A. J. Schofield, A. P. Mackenzie, M. Chiao, S. R. Julian, S. I. Ikeda, S. Nakatsuji, Y. Maeno, C. Pfleiderer, *Phys. Rev. Lett.* **2001**, *86*, 2661.
[11] G. Long, H. Henck, M. Gibertini, D. Dumcenco, Z. Wang, T. Taniguchi, K. Watanabe, E. Giannini, A. F. Morpurgo, *Nano Lett.* **2020**, *20*, 2452.

[12] Z. Wang, M. Gibertini, D. Dumcenco, T. Taniguchi, K. Watanabe, E. Giannini, A. F. Morpurgo, *Nat. Nanotechnol.* **2019**, *14*, 1116.
[13] Q. L. Pei, X. Luo, G. T. Lin, J. Y. Song, L. Hu, Y. M. Zou, L. Yu, W. Tong, W. H. Song, W. J. Lu, Y. P. Sun, *J. Appl. Phys.* **2016**, *119*, 043902.
[14] J. Lee, T. Y. Ko, J. H. Kim, H. Bark, B. Kang, S. G. Jung, T. Park, Z. Lee, S. Ryu, C. Lee, *ACS Nano* **2017**, *11*, 10935.
[15] M. J. Lee, S. Lee, S. Lee, K. Balamurugan, C. Yoon, J. T. Jang, S.-H. Kim, D.-H. Kwon, M. Kim, J.-P. Ahn, D. H. Kim, J.-G. Park, B. H. Park, *NPG Asia Mater.* **2018**, *10*, 23.
[16] S. Kim, J. Lee, G. Jin, M. H. Jo, C. Lee, S. Ryu, *Nano Lett.* **2019**, *19*, 4043.
[17] A. K. Budniak, N. A. Killilea, S. J. Zelewski, M. Sytnyk, Y. Kauffmann, Y. Amouyal, R. Kudrawiec, W. Heiss, E. Lifshitz, *Small* **2020**, *16*, 1905924.
[18] P. Gu, Q. Tan, Y. Wan, Z. Li, Y. Peng, J. Lai, J. Ma, X. Yao, S. Yang, K. Yuan, D. Sun, B. Peng, J. Zhang, Y. Ye, *ACS Nano* **2020**, *14*, 1003.
[19] R. Diehl, C.-D. Carpentier, *Acta Crystallogr., Sect. B: Struct. Crystallogr. Cryst. Chem.* **1977**, *33*, 1399.
[20] H. L. Zhuang, J. Zhou, *Phys. Rev. B* **2016**, *94*, 195307.
[21] M. Joe, H. Lee, M. M. Alyörük, J. Lee, S. Y. Kim, C. Lee, J. H. Lee, *J. Phys.: Condens. Matter* **2017**, *29*, 405801.
[22] K. Momma, F. Izumi, *J. Appl. Crystallogr.* **2011**, *44*, 1272.
[23] H. Li, S. Ruan, Y. J. Zeng, *Adv. Mater.* **2019**, *31*, 1900065.
[24] H. M. Rietveld, *Acta Crystallogr.* **1967**, *22*, 151.
[25] J. Rodríguez-Carvajal, *Phys. B* **1993**, *192*, 55.
[26] E. Ressouche, M. Loire, V. Simonet, R. Ballou, A. Stunault, A. Wildes, *Phys. Rev. B* **2010**, *82*, 100408.
[27] A. Louisy, G. Ouvrard, D. M. Schleich, R. Brec, *Solid State Commun.* **1978**, *28*, 61.
[28] C. C. Mayorga-Martinez, Z. Sofer, D. Sedmidubský, S. Huber, A. Y. S. Eng, M. Pumera, *ACS Appl. Mater. Interfaces* **2017**, *9*, 12563.
[29] L. Néel, *Proc. Phys. Soc., Sect. A* **1952**, *65*, 869.
[30] K. Yosida, *Prog. Theor. Phys.* **1951**, *6*, 691.
[31] T. Nagamiya, K. Yosida, R. Kubo, *Adv. Phys.* **1955**, *4*, 1.
[32] W. Zhang, K. Nadeem, H. Xiao, R. Yang, B. Xu, H. Yang, X. G. Qiu, *Phys. Rev. B* **2015**, *92*, 144416.
[33] B. Kuhlow, *Phys. Status Solidi A* **1982**, *72*, 161.
[34] M. A. McGuire, G. Clark, S. Kc, W. M. Chance, G. E. Jellison, V. R. Cooper, X. Xu, B. C. Sales, *Phys. Rev. Mater.* **2017**, *1*, 014001.
[35] S. Weyeneth, P. J. W. Moll, R. Puzniak, K. Ninios, F. F. Balakirev, R. D. McDonald, H. B. Chan, N. D. Zhigadlo, S. Katrych, Z. Bukowski, J. Karpinski, H. Keller, B. Batlogg, L. Balicas, *Phys. Rev. B* **2011**, *83*, 134503.
[36] M. D. Watson, A. McCollam, S. F. Blake, D. Vignolles, L. Drigo, I. I. Mazin, D. Guterding, H. O. Jeschke, R. Valentí, N. Ni, R. Cava, A. I. Coldea, *Phys. Rev. B* **2014**, *89*, 205136.
[37] T. Song, X. Cai, M. W.-Y. Tu, X. Zhang, B. Huang, N. P. Wilson, K. L. Seyler, L. Zhu, T. Taniguchi, K. Watanabe, M. A. McGuire, D. H. Cobden, D. Xiao, W. Yao, X. Xu, *Science* **2018**, *360*, 1214.
[38] D. R. Klein, D. MacNeill, J. L. Lado, D. Soriano, E. Navarro-Moratalla, K. Watanabe, T. Taniguchi, S. Manni, P. Canfield, J. Fernández-Rossier, P. Jarillo-Herrero, *Science* **2018**, *360*, 1218.
[39] D. R. Klein, D. MacNeill, Q. Song, D. T. Larson, S. Fang, M. Xu, R. A. Ribeiro, P. C. Canfield, E. Kaxiras, R. Comin, P. Jarillo-Herrero, *Nat. Phys.* **2019**, *15*, 1255.
[40] Y. Deng, Y. Yu, M. Z. Shi, Z. Guo, Z. Xu, J. Wang, X. H. Chen, Y. Zhang, *Science* **2020**, *367*, 895.
[41] C. Liu, Y. Wang, H. Li, Y. Wu, Y. Li, J. Li, K. He, Y. Xu, J. Zhang, Y. Wang, *Nat. Mater.* **2020**, *19*, 522.
[42] B. Chen, F. Fei, D. Zhang, B. Zhang, W. Liu, S. Zhang, P. Wang, B. Wei, Y. Zhang, Z. Zuo, J. Guo, Q. Liu, Z. Wang, X. Wu, J. Zong, X. Xie, W. Chen, Z. Sun, S. Wang, Y. Zhang, M. Zhang, X. Wang, F. Song, H. Zhang, D. Shen, B. Wang, *Nat. Commun.* **2019**, *10*, 4469.
[43] G. Kresse, J. Furthmüller, *Comput. Mater. Sci.* **1996**, *6*, 15.
[44] J. P. Perdew, K. Burke, M. Ernzerhof, *Phys. Rev. Lett.* **1996**, *77*, 3865.
[45] P. E. Blöchl, *Phys. Rev. B* **1994**, *50*, 17953.